ARTICLES

Differential Pulse and Chronoamperometric Studies of Insonated Systems: Acoustic Streaming and Cavitational Effects

F. Javier Del Campo, James Melville, Joanna L. Hardcastle, and Richard G. Compton*

Physical & Theoretical Chemistry Laboratory, Oxford University, South Parks Road, Oxford OX1 3QZ, U.K.

Received: August 15, 2000; In Final Form: November 14, 2000

Chronoamperometry has been undertaken at insonated electrodes of both micro and macro dimensions, for a range of simple, well-defined redox couples in water (298 K), DMF (298 and 218 K), and ammonia (218 K) as solvents. These are analyzed to assess the relative contributions of acoustic streaming and cavitational activity to the observed currents: both contribute significantly under the usual conditions adopted for sonovoltammetry. Differential pulse voltammetry (DPV) was then used to explore the nature of the diffusion layer prevailing under steady-state electrolysis of insonated macroelectrodes. Simulations showed that pure convection within a diffusion layer enhances the DPV currents for simple redox systems as compared to silent conditions. The experimentally observed decrease was attributed to cavitational disruption of the diffusion layer leading to a physical model of an insonated electrode which may be described as a steady diffusion layer a few microns thick brought about by acoustic streaming which is occasionally and randomly punctuated by a cavitational event. The frequency and violence of the event is dependent on the solvent and ultrasound power, except at very short electrode-to-horn separation where the cavitational contribution becomes substantial.

1. Introduction

Sonoelectrochemistry is a fast developing discipline[1] which has already evolved significant applications in the areas of sonoelectrosynthesis,[2−8] and sonoelectroanalysis[9−13] as well as niche use in electroplating[14] and metal recovery.[15,16] On a fundamental level, the often dramatic increase in mass transport limited currents seen on insonation using 20 kHz ultrasound is attributed as arising from both cavitational phenomena[17,18] and acoustic streaming.[19] Cavitation is caused by the collapse of voids created by ultrasonic compression and rarefaction of the solution and results in localized high pressures and temperatures throughout the bulk solution.[20] Figure 1b shows the asymmetric collapse of cavitational bubbles at an electrode (or other) surface leads to microjetting with jet speeds up to ca.100 cm s^{-1}.[21] In voltammetry, microjetting is revealed as sharp current spikes superimposed on any background response. Acoustic streaming[22] is a nonlinear effect that allows high-intensity sound energy to be converted into kinetic energy in the liquid surrounding the sound source, as shown in Figure 1a. The resulting turbulent solution flow can give rise to significant sustained currents at electrodes in either the "face-on" mode with respect to sonic horn or as sonotrodes. The difference between these two configurations is illustrated in Figure 2.

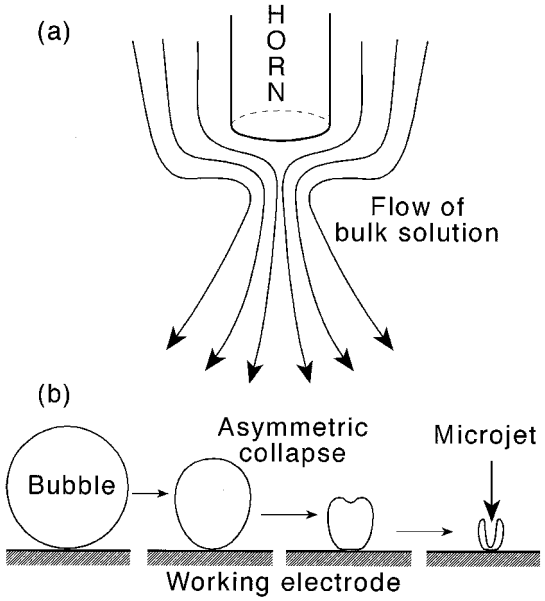

Figure 1. (a) Representation of acoustic streaming. (b) An ultrasonically induced cavitational bubble collapsing in the vicinity of a surface.

In this paper we assess the relative contributions of acoustic streaming and cavitationally induced microjetting to the sonovoltammetric response of well-characterized simple redox couples measured in the solvents water, dimethylformamide (DMF), and ammonia. The wide liquid range of DMF (T_m = −60 °C, T_b = 156 °C) permits comparative data to be obtained at temperatures similar to those used both for the water and ammonia based systems. In addition to simple voltammetric data recorded under transport limited currents at both micron and millimeter dimensioned electrodes, we make use of differential pulse voltammetry as a sensitive means of exploring the nature of the diffusion layer prevailing under steady-state electrolysis at insonated electrodes. The potential sequence of defining this form of voltammetry is shown in Figure 3. The current is measured immediately before each pulse is applied and again at the end of the pulse; the difference between the two currents

10.1021/jp002948l CCC: $20.00
Published on Web 12/30/2000

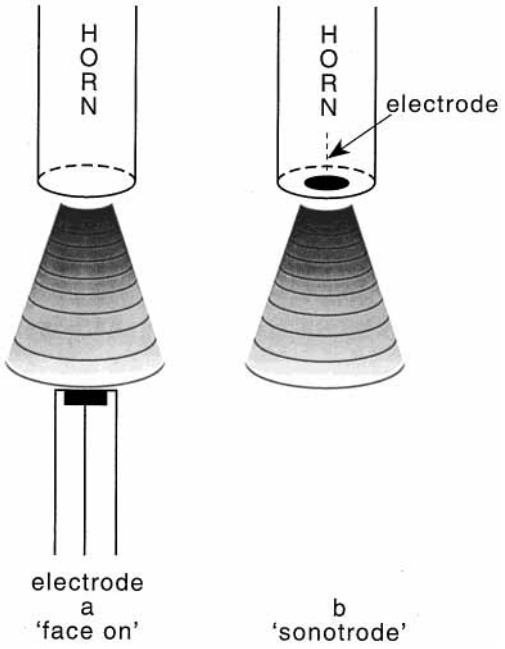

Figure 2. Possible electrode geometries for sonovoltammetry; (a) "face-on" positioning and (b) diagram of a sonotrode.

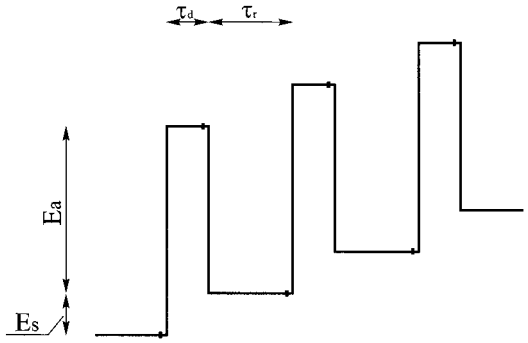

Figure 3. Potential waveform of the DPV experiment, formed by the superposition of two waveforms, a staircase waveform and a pulse waveform. Ea represents the amplitude potential, Es the step potential, τ_d is the duration of the pulse, and τ_r is the duration of the "rest" period between pulses.

is recorded as a function of the voltage on the underlying staircase. Given that it is a difference in current which is monitored, it follows that the technique will be sensitive to the transport conditions prevailing during the interval between current sampling times. In particular, in a cavitation free sonovoltammetric experiment it would be expected[23−25] that a diffusion layer would be established in which convection was reduced as compared to bulk solution. The transport of material within this diffusion layer would therefore control the DPV response. However, in a cavitationally highly active situation, the frequent disruption of the diffusion layer by bubble activity would reduce the voltammetric sensitivity if the frequency is such that bubbles are regularly formed in the time period between sampling times.

In the following we explore the effect of convection on the DPV response, considering first the limit of a Nernstian diffusion layer in which the solution is fully stagnant and second the use of a rotating disk electrode where the influence of well-defined convection with the diffusion layer can be quantified. The results of this theoretical investigation permit the resolution of convective and cavitational effects in sonovoltammetry via the experiments reported later in this paper.

2. Simulation Theory

The theory of DPV is considered for the following electrochemically reversible redox reaction at a uniformly accessible electrode

$$\mathrm{RED} \leftrightarrow \mathrm{OX} + \mathrm{e}^- \tag{1}$$

The current generated during a DPV experiment is given by

$$I = FAJ \tag{2}$$

where A is the area of the electrode, J is the flux to the electrode defined as

$$J = D_{\mathrm{R}}\left(\frac{\partial[\mathrm{RED}]}{\partial y}\right)_{y=0} \tag{3}$$

and y is the Cartesian coordinate normal to the electrode surface.

Theory will first be considered for the case of a Nernst diffusion layer, of thickness δ, in which transport is by diffusion alone and outside of which concentrations are maintained at "bulk" values. In this case, the concentration of RED and OX is calculated by applying Fick's second law of diffusion

$$\frac{\partial[\mathrm{RED}]}{\partial t} = D_{\mathrm{RED}}\frac{\partial^2[\mathrm{RED}]}{\partial y^2} \tag{4}$$

$$\frac{\partial[\mathrm{OX}]}{\partial t} = D_{\mathrm{OX}}\frac{\partial^2[\mathrm{OX}]}{\partial y^2} \tag{5}$$

These equations are solved and concentrations of RED and OX obtained throughout the diffusion layer. To solve the equations, boundary conditions are required. The first of these is that initially, the potential is set so that the RED/OX equilibrium lies far to the RED side. In practical terms this means that the concentration of RED is at its bulk value and the concentration of OX is zero everywhere. Algebraically, at $t = 0$, $0 < y < \delta$,

$$[\mathrm{RED}] = [\mathrm{RED}]_{\mathrm{bulk}} \qquad [\mathrm{OX}] = 0 \tag{6}$$

The second boundary condition specifies that the concentration of RED will tend toward its bulk value beyond the edge of the diffusion layer, while that of OX will be zero. At $t > 0$, $y = \delta$,

$$[\mathrm{RED}] = [\mathrm{RED}]_{\mathrm{bulk}} \qquad [\mathrm{OX}] = 0 \tag{7}$$

At the electrode surface, the redox reaction is assumed to be reversible and therefore the concentrations of RED and OX are given by the Nernst equation at $t > 0$, $y = 0$

$$\frac{[\mathrm{OX}]_0}{[\mathrm{RED}]_0} = \mathrm{e}^{\theta} \tag{8}$$

where

$$\theta = \frac{F}{RT}(E - E^{0'}) \tag{9}$$

and $E^{0'}$ is the formal potential of the redox couple. E is the potential at time t, given by the following equation:

$$E = \begin{cases} E_0 + (t-1)\mathrm{Es}/2 & t = 1, 3, 5... \\ E_0 + (t-2)\mathrm{Es}/2 + \mathrm{Ea} & t = 2, 4, 6... \end{cases} \tag{10}$$

where E_0 is the initial potential and Es and Ea are the step potential and amplitude potential of the DPV waveform, defined in Figure 3.

The final boundary condition specifies conservation of flux at the electrode surface when $t > 0$ and $y = 0$

$$D_{ox}\frac{\partial[OX]}{\partial y} = -D_{RED}\frac{\partial[RED]}{\partial y} \tag{11}$$

Computer solutions to these equations were obtained by use of the finite difference backward implicit (BI)[26−28] method with a back-to-back grid. A full explanation of the procedure is given elsewhere[29] and involves dividing the diffusion layer into 2NJ + 1 points, where NJ is an integer. These points are then labeled by the coordinate *j*. The values of RED are stored at values of *j* from 0 to NJ, the values of OX are stored at the equivalent grid points in negative space, i.e., from −1 to −NJ. A spatial coordinate transform[30] is employed to increase the efficiency of the simulation.

In the simulations, the diffusion layer thickness can be set to a value large enough that a semi-infinite diffusion layer effectively pertains (e.g., 300×10^{-4} cm) or to finite values, for example those which might be created due to the action of ultrasound or rotation of an electrode. With these parameters specified and the boundary conditions in place, time-dependent[31,32] solutions of the mass transport equations can be obtained by the BI method.

In the case of an experiment using a rotating disk electrode, a convective term is added to the equations describing the mass transport behavior of RED and OX.[33]

$$\frac{\partial[RED]}{\partial t} = D_{RED}\frac{\partial^2[RED]}{\partial y^2} + Cy^2\frac{\partial[RED]}{\partial y} \tag{12}$$

$$\frac{\partial[OX]}{\partial t} = D_{ox}\frac{\partial^2[OX]}{\partial y^2} + Cy^2\frac{\partial[OX]}{\partial y} \tag{13}$$

where Cy^2 is the convection term normal to and close to the electrode. The constant *C* is given by

$$C = 8.032\, W^{3/2}\, \nu^{-1/2} \tag{14}$$

where *W* is the speed of rotation of the disk in Hz, and ν is the kinematic viscosity in units of $cm^2\ s^{-1}$.

The diffusion layer thickness that is created by the motion of the RDE is predicted by the following equation:[34]

$$\delta = 0.643\, \nu^{1/6}\, D_{RED}{}^{1/3}\, W^{-1/2} \tag{15}$$

A coordinate transform, based on the Hale transformation,[33,35,36] was also used to improve the efficiency of the simulation. The same boundary conditions apply as for the nonconvective simulation, and the mass transport equations are solved in a similar fashion.

The simulations were compiled using FORTRAN 77 and executed on a Silicon Graphics Origin 2000 server, except the equation involved in the Hale transformation, which was solved using Matlab v.5.1.0.421.

3. Theoretical Implementation and Results

The accuracy of the computer simulation depends on the two parameters: NJ, the number of spatial points over which the equations are solved (the larger NJ, the finer the grid, and hence the more accurate the results) and NL, the number of times at each DPV pulse or rest period, the calculations are carried out.

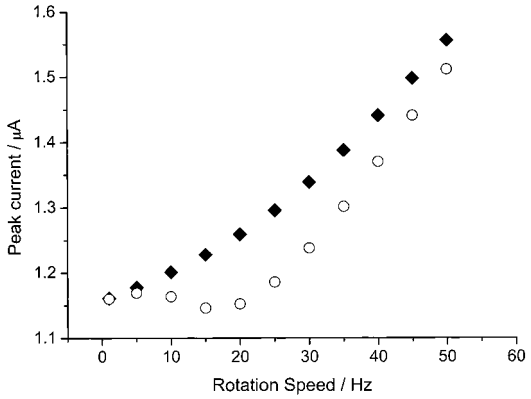

Figure 4. Results for the simulation of DPV of the reduction of $Ru(NH_3)_6^{3+}$ in water at (○) a static electrode and (◆) a rotating disk electrode. Radius of electrode = 5.00×10^{-2} cm, $T = 298$ K, kinematic viscosity = 10^{-2} $cm^2\ s^{-1}$, scan between −0.3 V to 0.0 V, Ea = 0.01995V, Es = 0.00195 V, $\tau_d = 0.05$ s, $\tau_r = 0.1$ s, initial concentration of $Ru(NH_3)_6^{3+} = 10^{-6}$ mol cm^{-3}, diffusion coefficient of $Ru(NH_3)_6^{3+}$ = diffusion coefficient of $Ru(NH_3)_6^{2+} = 9.1 \times 10^{-6}$ $cm^2\ s^{-1}$, $E° = -0.171$ V, NJ = 500, NL = 500. In the case of a static electrode, diffusion layers were set equal to the values that would be expected at a specific disk rotation speed by eq 15.

The simulation was first run at extremely high NJ and NL values (= 10000 points) to ensure that the result obtained was free from any errors due to the coarseness of either temporal or spatial measurements. The number of points was then reduced until the simulation ran within 99% accuracy of these results, at NJ and NL = 500. This resulted in the simulations running within an acceptable time (approximately 3 min for each voltammogram).

The simulation of DPV at a RDE was run under physical conditions that applied to the reduction of $Ru(NH_3)_6^{3+}$ in water. The parameters used were $T = 298$ K, kinematic viscosity = 10^{-2} $cm^2\ s^{-1}$, scan between −0.3 V to 0.0 V, Ea = 0.01995V, Es = 0.00195 V, $\tau_d = 0.05$ s, $\tau_r = 0.1$ s, initial concentration of $Ru(NH_3)_6^{3+} = 10^{-6}$ mol cm^{-3}, diffusion coefficient of $Ru(NH_3)_6^{3+}$ = diffusion coefficient of $Ru(NH_3)_6^{2+} = 9.1 \times 10^{-6}$ $cm^2\ s^{-1}$,[37] $E^{0\prime} = -0.171$ V. The radius of the electrode used was nominally set as 5.00×10^{-2} cm, to directly compare with results obtained with a static electrode. It should be noted that this is not the size of a practical RDE, but the currents simply scale with the area of the electrode. The computational parameters used were NJ = 500, NL = 500. The frequency of disk rotation was varied from between 1 and 50 Hz.

Figure 4 shows the variation of peak current with rotation speed for a rotating disk (i) having a diffusion layer given by eq 15 and (ii) a Nernstian diffusion layer of the same length, δ.

The results were plotted to show the change in peak current against the rotation speed of the RDE required to achieve the relevant diffusion layer thickness, as predicted by eq 15. The general trend is as the speed of rotation increases (which corresponds to a reduction in diffusion layer thickness in the static simulation), the peak height increases, due to convection increasing mass transport to the electrode.

Turning to sonovoltammetry the simulations predict, by analogy, that at a given diffusion thickness, if the main effect of sonication is an enhancement of mass-transfer to the electrode via convection from acoustic streaming, a larger peak current will flow than that which would be measured under pure, entirely stagnant, "Nernstian" diffusion layer conditions.

4. Experimental Section

4.1. Reagents and Instrumentation. Chemical reagents used were as follows: ammonia (BOC) KI (AnalaR, 99.8%), lithium

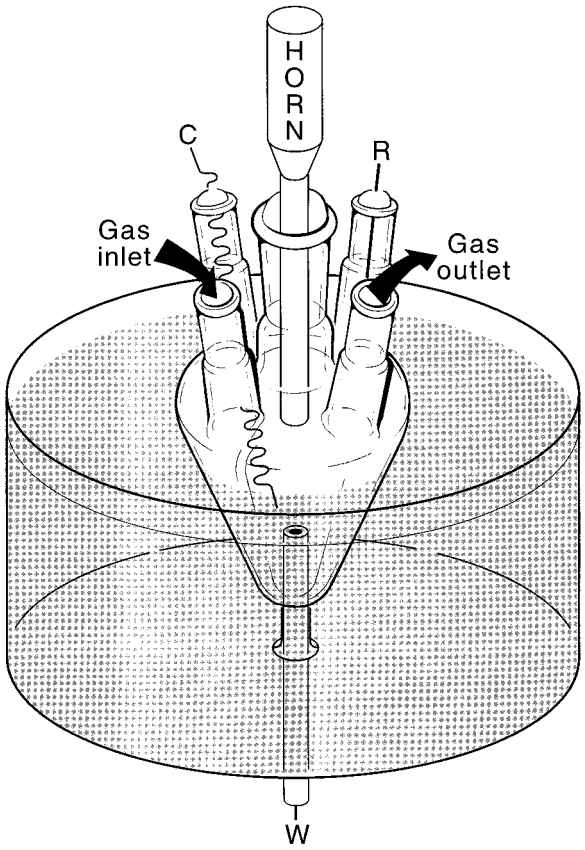

Figure 5. Electrolytic cell used for the experiments described.

wire (Aldrich, 99.9%), nitrotoluene (Aldrich, 99+%). DMF (Aldrich, 99.9+% HPLC grade), tetrabutylammonium hexafluorophosphate (Fluka, electrochemical grade), ferrocene (Aldrich, 98%), hexamine ruthenium chloride (Aldrich 98%), potassium chloride (Fluka 99+%). Argon (Pureshield, BOC) was used to maintain a dry and inert atmosphere. Aqueous solutions were prepared using UHQ grade water of resistivity of not less than 18 MΩcm (Elga, High Wycombe, Bucks, UK).

The working electrode used was either a macro (1 mm) or micro (50 μm) Pt disk electrode mounted in glass. Teflon was avoided as electrode shrouding material due to its large coefficient of thermal expansion, which caused the Pt electrode to protrude in low-temperature experiments, thus exposing an unknown surface area.

The working electrode was polished prior to measurements using alumina lapping compounds (BDH or Microglass Instruments, Greensborough, Victoria 3088, Australia) of increasing grade down to 0.05 μm particle size. A gold foil served as the counter electrode, and a silver wire (Aldrich, 99.9% 0.5 mm diameter) was used as a pseudoreference electrode in ammonia and DMF. In aqueous solution, all potentials are quoted with respect to the saturated calomel electrode, (SCE, Radiometer, Copenhagen). Thermostating of the electrochemical cell (see Figure 5) was accomplished by means of an ethanol−dry ice mixture, which allowed experiments to be conducted over a wide range of low temperatures (from −60 °C up to room temperature). An ultrasound horn transducer system (Sonics & Materials, VCX400) with a stepped 3 mm diameter tip horn (titanium alloy) was employed. The horn probe was electrically insulated and positioned 'face-on'[37] toward the working electrode with a variable distance ranging from 2 millimeters up to 2 cm. All experiments were performed using a computer controlled Autolab PGSTAT 20 system (Eco Chemie, Utrecht, Netherlands).

4.2. Experimental Procedure. In the case of liquid ammonia and DMF electrochemical experiments were carried out under dry conditions in an inert atmosphere of argon. This is especially important in liquid ammonia, where traces of water may preclude meaningful voltammetric measurement. The supporting electrolyte in ammonia, KI, was pretreated by grinding into a fine powder and drying in an oven at 130−140 °C overnight. The electrodes were kept in a desiccator. The ammonia was dried by first condensing it into a flask containing pieces of lithium. Then, 50 mL was distilled under argon into the electrochemical cell containing the supporting electrolyte, KI.

For the experiments conducted in DMF and in water, the same experimental setup was used. To reach the low temperatures required for some of the experiments described below, a mixture of dry ice and ethanol was used to bathe the electrochemical cell. The temperatures were stable within a two degree Celsius range. It is well known that prolonged use of power ultrasound unavoidably causes the temperature to increase. Time was allowed between data collection in order to ensure the same starting temperature conditions for each voltammetric measurement recorded.

The diffusion coefficient for ferrocene in DMF at low temperature was determined by means of a series of potential step experiments at a microelectrode (50 μm) under silent conditions and at different temperatures. The diffusion coefficient was found to behave according to an Arrhenius-type relation. A plot of ln$D$ vs $1/T$ for diffusion in DMF gave an activation energy of 10500 J/mol. This allows the calculation of diffusion coefficient at any required temperature using eq 16.

$$D_{T2} = D_{T1}\left[\frac{E_a}{R}\left(\frac{1}{T_1} - \frac{1}{T_2}\right)\right] \tag{16}$$

D_{T2} is the diffusion coefficient in m^2s^{-1} at the desired Kelvin temperature, T_2, D_{T1} is the known diffusion coefficient for that species at a given Kelvin temperature, T_1, E_a is the activation energy for diffusion in J mol^{-1} in a particular solvent (in this case DMF), and R is the gas constant.

The ultrasonic intensity was calibrated calorimetrically in water and room-temperature DMF according to the procedure of Margulis et al.[38] over the range 40−550 Wcm^{-2}. The calibration of the ultrasonic horn under low-temperature conditions has been described.[39] To achieve different diffusion layer thicknesses, for the DPV experiments, both the distance between the ultrasonic horn and the electrode and the input power were changed according to need.

The differential pulse voltammetry (DPV) parameters typically employed were amplitude potential, Ea, 0.025 V, step potential, Es, 0.00495 V, modulation time, τ_d, 0.05 s, and rest time, τ_r, 0.1 s. Time-resolved experiments were conducted at both macro and micro electrodes under the presence of power ultrasound. The duration of the experiments ranged from 100 ms up to 500 ms, the time scale resolution of the experiments being 50 μs. This allowed us to observe single cavitational collapses at the microelectrode (see below). In this set of experiments, typical ultrasonic probe-electrode distances were 5, 10, and 15 mm.

5. Experimental Results and Discussion

We consider first current−time measurements recorded at a 50 μm diameter platinum electrode in ammonia, water, and DMF (at 298 and 218 K). In each case a well-characterized simple one electron redox couple was employed as given in

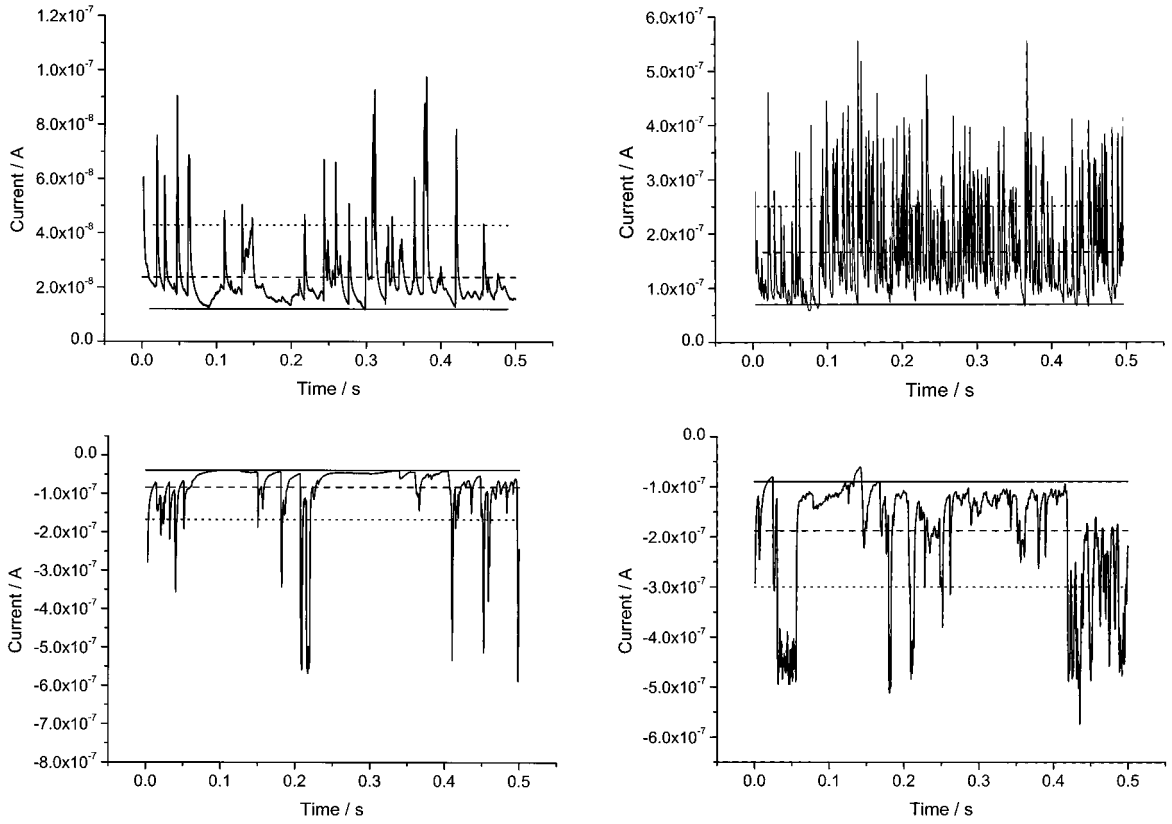

Figure 6. Chronoamperometric experiments at a 50 μm diameter Pt disk in the presence of ca. 250 Wcm^{-2} ultrasound in different media and temperatures: (a) 1 mM ferrocene in DMF at 218 K, (b) 1 mM ferrocene in DMF at 298 K, (c) 1 mM $Ru(NH_3)_6^{3+}$ in water at 20 °C, (d) 1 mM nitrotoluene in liquid ammonia at 218 K. The additional lines superimposed on the traces correspond to the calculated baseline current (—) calculated average current (-----) and standard deviation (...).

TABLE 1: Redox Systems Studied at a 50 μm Platinum Disk Electrode under Silent Conditions

solvent	redox system	supporting electrolyte	silent current/nA	D/cm^2 s^{-1}	$E_{1/2}$/V
NH_3	nitrotoluene	KI	18	1.4×10^{-5}	−0.390 vs Ag
H_2O	$Ru(NH_3)_6^{3+}$	KCl	13	9.1×10^{-6}	−0.171 vs.SCE
DMF (298 K)	ferrocene	TBAHFP	12	1.2×10^{-5}	0.470 vs Ag
DMF (218 K)	ferrocene	TBAHFP	4	2.6×10^{-6}	0.774 vs Ag

Table 1. For all experiments the electrode was held at a potential corresponding to the transport limited electrolysis of the substrate of interest. Under silent conditions, steady, near constant currents were observed consistent with the equation

$$I_{\text{lim}} = 4nFDcr \tag{17}$$

and the diffusion coefficients given in Table 1. Note that the currents are of the order of several nanoamperes. With insonation, the current−time behavior for the same systems is shown in Figure 6. We consider first Figure 6a which shows the behavior found in DMF at 218 K. Sharp spikes are evident, superimposed on a background current that is much enhanced in comparison with the steady-state current seen under silent conditions. The average current and the estimated background current are shown in Figure 6a together with an indication of the magnitude of the standard deviation. The spikes are caused by the collapse of single cavitational bubbles in the vicinity of the electrode. When a cavitational bubble collapses near the electrode surface, a jet of electrolyte is cast against it, bringing new electroactive material and thus giving an enhanced current. This way, one can record direct hits or near misses of these microjets of solution as individual current transients of differing height and shape. Therefore, for a microjet impinging directly on the electrode surface, the current observed in the corresponding spike may be higher than if the jet had hit the edge of the electrode. These observations and inferences are consistent with the work of Birkin,[21] Degrand,[40] and Alkire.[41,42]

Figures 6b, 6c, and 6d show experiments analogous to those reported for DMF at 218 K but correspond to DMF and water at 298 K, and ammonia at 218 K. Again the traces are annotated to show the estimated "background" current and the standard deviation. Comparison of the former with the "silent" limiting currents reported in Table 1 reveal a substantial increase under all conditions, indicating that acoustic streaming contributes measurably to the mass transport resulting in a steady convective flow augmenting that from diffusion to the microelectrode. However comparison of "baseline" and "average" currents show a significant contribution from cavitation in all cases.

Comparing figures 6a, 6b, 6c, and 6d, the frequency and violence of cavitational events are different from one medium to the next. This reflects differences in physical properties between solvents, primarily the vapor pressure and viscosity. These parameters are reported in Table 2. It is possible to assess what is termed the "violence" of imploding of cavitational bubbles by observing surface erosion and the limiting current of insonated redox processes when physical conditions promote an increase in the force of cavitational collapse. The violence of each cavitational event is known to change with both applied

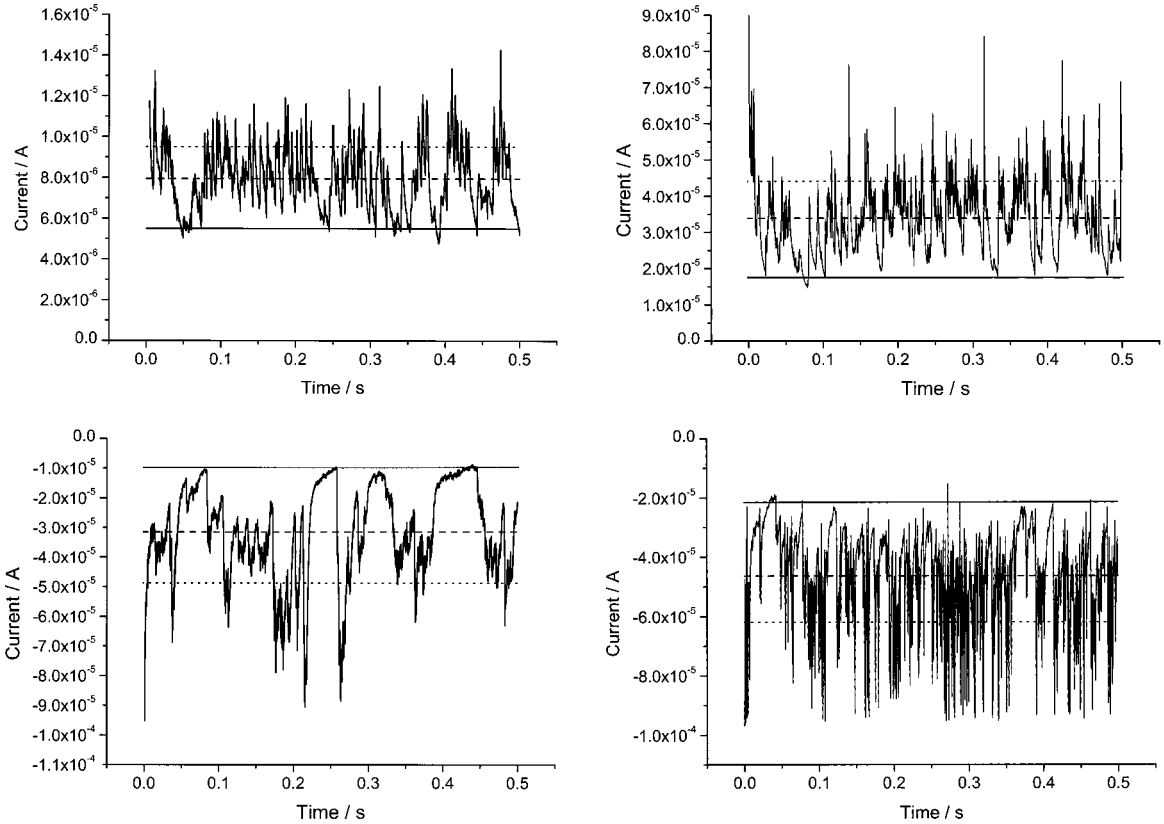

Figure 7. Chronoamperometric experiments at a 1 mm diameter Pt disk in the presence of ca. 250 Wcm^{-2} ultrasound in different media and temperatures: (a) 1 mM ferrocene in DMF at 218 K, (b) 1 mM ferrocene in DMF at 298 K, (c) 1 mM $Ru(NH_3)_6^{3+}$ in water at 298 K °C, (d) 1 mM nitrotoluene in liquid ammonia at 218 K. The additional lines superimposed on the traces correspond to the calculated baseline current (—) calculated average current (-----) and standard deviation (...).

TABLE 2: Vapor Pressure and Viscosity Data[a,b,c]

	218 K	298 K		
solvent	NH_3	water	DMF	DMF
vapor pressure/mmHg	200	24	4	2
viscosity/cP	0.4	0.9	0.95	1.0

[a] Lide D. R. (Ed.) *CRC Handbook of Chemistry and Physics 74th Edition*; CRC Press: Boca Raton, Florida, 1993. [b] Boublík T, Fried V., Hála E. *The Vapor Pressure of Pure Substances;* Elsevier Science B. V.: Amsterdam, The Netherlands, 1984. [c] Corradini F., Marchetti A., Tagliazucchi M., Tassi L., Tosi G., *Can. J. Chem. Eng.*, **1993**, *71*, 124.

pressure[43,44] and vapor pressure.[44] It is thought that cavitational bubbles are allowed to grow larger in media of high vapor pressure,[43] and therefore when the bubble collapses the implosion is less violent due to the cushioning effect arising from its larger size. This has been termed "soft cavitation".[44] Large bubbles may also have greater opportunity to move away from the surface of the electrode. Conversely sonication within a solvent of low vapor pressure brings about much more violent cavitational events.[43] In this case more energy is required to disrupt the medium in order to create a void. The bubbles formed are therefore much smaller, reducing the "cushioning effect". The chance of these small bubbles escaping from the surface is lessened, and the resulting cavitational collapses become not only more frequent but also violent. In water and liquid ammonia (Figure 6c, d), where vapor pressure is higher, fewer spikes are observed than in DMF at 298 K possibly because bubbles are allowed to grow large enough to rise up and leave the solution without collapsing. Greater stability of bubbles in the solvent with the highest vapor pressure (ammonia) is also evident (Figure 6d) where a broad cluster of spikes during the first 50 μs may be interpreted as oscillation of a large bubble. The viscosity of the solvent is also a contributing factor to the nature of the observed cavitation. A comparison of Figure 6a, b demonstrates that although the vapor pressure of DMF is lower at 218 K than at 298 K the violence and frequency of cavitation do not increase. The peak sizes are in fact much smaller and less frequent in the low-temperature case. The viscosity of DMF at low temperature is higher than at room temperature, and a possible result is the much less efficient replacement of solution at the electrode surface on cavitational collapse and therefore a smaller current enhancement when the microjet impinges on the surface. The frequency of cavitational collapse is reduced in comparison with the higher temperature case due to the increased energy required to create a void in the more viscous solution of low vapor pressure.

Macroelectrode (1 mm diameter Pt disk) experiments were conducted in which current−time measurements were recorded in water (298 K), DMF (298 and 218 K), and NH_3 (218 K) in the presence of ultrasound. The electrode was held at potentials such that reduction (nitrotoluene in NH_3 and $Ru(NH_3)_6^{3+}$ in water) or oxidation (ferrocene in DMF) of electroactive species was controlled by mass transport. The observed current traces are shown in Figure 7. In this set of experiments, three ultrasonic probe−electrode distances were used (5, 10, and 15 mm; see Table 3), but the ultrasonic power employed remained constant at around 250 Wcm^{-2}. Although the traces resemble those from the microelectrode experiments, there is a noticeable difference between them. Those obtained at the macroelectrode are much "noisier" than their microelectrode counterparts, regardless of the medium. It is still possible to see sharp spikes for the case of DMF, and the presence of large oscillating bubbles in water and ammonia may also be inferred. The spikes, however, no

TABLE 3: Currents Obtained at a 1 mm Pt[a]

solvent	horn-electrode distance/mm	T/K	baseline/μA	average current/μA	standard deviation[b]/μA	diffusion layer[c]/μm
	5		20.4	38	12.4	5.2
NH_3	10	218	17.5	28.9	17.2	6.1
	15		16.2	25.8	8.6	6.5
	5		4.42	6.1	1.78	4.5
DMF	10	218	2.84	4.25	1.42	6.9
	15		1.89	2.71	1.15	10.4
	5		18.1	26.7	6.76	5
DMF	10	298	9.34	18.1	12.2	9.7
	15		9.22	12.6	7.3	9.9
	5		21.7	32.9	5	3.2
H_2O	10	298	13	17.2	4.1	5.3
	15		11.4	16.3	6.4	6.1

[a] Electrode under 250 Wcm^{-2} ultrasound in different media. Diffusion layer thicknesses have been calculated using eq 18 and *D* values given in Table 1. [b] Relating to the average current. [c] Values calculated using the base current in eq 18.

longer correspond to single events but relate to a multiplicity of collapses occurring at closely similar times. Single cavitational bubbles grow no bigger than a 15 to 20 μm with a Sauter mean diameter of 10 μm.[45] Hence the current arising from one of these microjets can go almost unnoticed at an electrode of millimeter dimensions due to the magnitude of the overall current. The sonoocurrents at the macroelectrode (Figure 7) are the order of microamps, while the currents caused by single cavitational collapses (Figure 6) are the order of nanoamps. In addition, given that the area of the macroelectrode is ca. 400 times larger than the microelectrode, it is reasonable to conclude that at a macroelectrode more than one event will happen at the same time on the surface, given the frequency of single bubble events recorded on the microelectrode.

The baseline currents shown in Figure 7 were estimated and can be attributed to the effect of acoustic streaming alone. These currents were then used to calculate the diffusion layer thicknesses quoted in Table 3 using eq 18, which presumes a simple Nernstian diffusion layer model.

$$I_{\mathrm{lim}} = \frac{nFADc}{\delta} \tag{18}$$

In this equation I_{lim} is the baseline current, *A* the electrode area, *F* the Faraday constant, and *c* the bulk concentration. Table 3 also contains the average current and standard deviation values as defined in Figure 7. The contribution of cavitation to the traces such as in Figure 7 may be quantified by two factors: the standard deviation of the current from the average current, and the difference between the baseline current and the average current. Both factors follow the same trend as they do for the microelectrode case discussed above. In particular the relative contribution of cavitation decreases as the electrode-to-horn separation increases, consistent with the known localization of cavitational events near to the tip of the sonic horn. However, on examining Figure 7 it is important to observe the "multiplet" nature of the spikes recorded at a macroelectrode contrasting with the discrete spikes observed in the case of a microelectrode. One can infer from this that a multitude of stable oscillating bubbles[46] on the surface contribute to the observed transient. This highlights the difficulties in quantifying cavitation at a macroelectrode.

We next report the use of DPV as a sensitive means of probing the physical nature of the diffusion layer prevailing at an insonated macroelectrode to facilitate assessment of the relative contributions of acoustic streaming and cavitation in different media. Linear sweep voltammograms at a scan rate of 25 mVs^{-1} were recorded using a 1 mm platinum macroelectrode

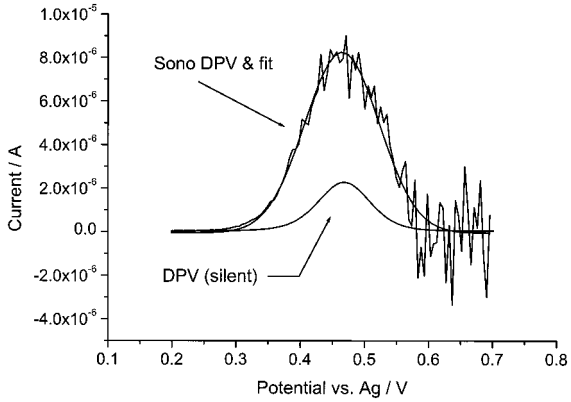

Figure 8. (a) Sono-DPV of 1 mM ferrocene in DMF at 20 °C in the presence of ca. 250 Wcm^{-2} ultrasound. (b) Comparison between sono and silent DPV of 1 mM ferrocene in DMF at 20 °C.

electrode in a face on arrangement with an ultrasonic horn at a range of ultrasound powers from 50 to 500 Wcm^{-2} and horn-to-electrode separations of 2 to 15 mm for the simple redox couples described in Table 1. Determination of the baseline currents allowed eq 18 to be employed to calculate the diffusion layer thickness associated with a stagnant diffusion layer for each combination of horn electrode separation and power. The results of this calibration gave a range of diffusion layer thicknesses from ca. 7 μm down to ca. 0.5 μm, which could be effected by a known combination of horn to electrode separation and ultrasound power in each solvent.

Differential pulse voltammograms were then recorded with modulation amplitude 0.025 V, step height 0.00495 V, modulation time 0.05 s, and rest time 0.1 s, for an insonated 1 mm platinum electrode over the range of diffusion layer thicknesses calibrated. Figure 8 shows a typical sono-DPV voltammogram for ferrocene in DMF at 298 K. The "noisy" data were fitted to the Gaussian form typical of a silent voltammogram using Origin 6.0 (Microcal, MA), which allowed the detemination of the peak current in each of the insonated cases. Note the enhancement of the signal in Figure 8 as compared to silent conditions.

Simulation of DPV as outlined in section 2 was used to calculate the theoretical peak current for each of the diffusion layer thicknesses (estimated as described above) in the insonated experiment. Given the assumption made in the theory, we estimate that the theoretical predictions are likely to be accurate to within 5 to 10%.[44] The parameters of the DPV simulation corresponded to those employed experimentally. Figure 9 (a−d) shows a comparison of experimental peak currents and theoretical peak currents for the solvents DMF, water and ammonia at a range of diffusion layer thicknesses.

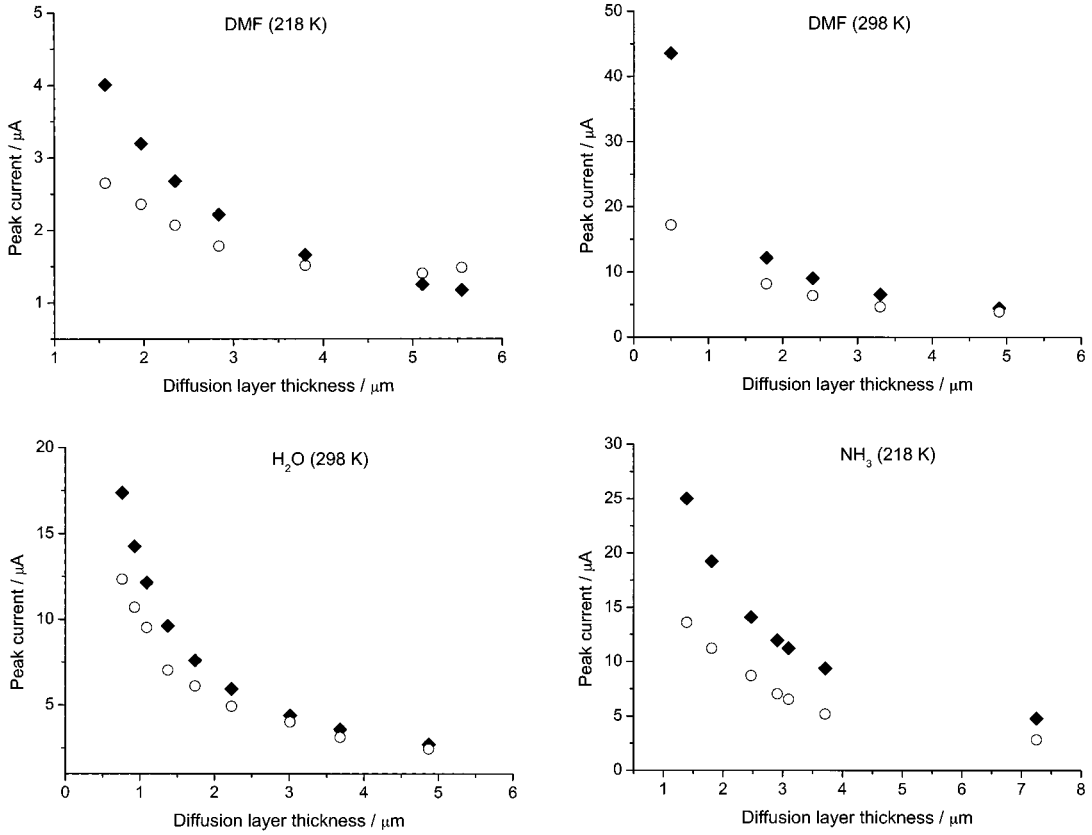

Figure 9. Theoretical stagnant Nernst diffusion model (◆) and experimental (○) DPV peak currents for (a) 1 mM ferrocene in DMF at 218 K, (b) 1 mM ferrocene in DMF at 298 K, (c) 1 mM $Ru(NH_3)_6^{3+}$ in water at 20 °C, (d) 1 mM nitrotoluene in liquid ammonia at 218 K.

It is evident from Figure 9 that experimentally obtained peak currents are smaller than those theoretically predicted at a given diffusion layer thickness, deviating most markedly at small diffusion layer thicknesses where the ultrasonic perturbation is greatest. It was predicted from the simulations for the rotating disk reported above that the increasing mass transport via pure convection (higher rotation speeds) would lead to a larger peak current than that which would be measured under "Nernstian" diffusion layer conditions. It is therefore likely that cavitation, not acoustic streaming, is responsible for this deviation due to the turbulent collapse of bubbles perturbing or even replacing the diffusion layer. The conditions where we believe cavitation is strongest (described for the microelectrode transients) result in the greatest deviation between theory and experiment. For all of the solvents, the largest deviation is observed at the smallest diffusion layer thickness, corresponding to the smallest horn to electrode separation and highest power of ultrasound. A comparison of the extent of the deviation across the different solvents presents the largest deviation for DMF at 298 K and the smallest deviation for DMF at 218 K. These observations follow a trend consistent with the frequency and violence of cavitation shown in the chronoamperometry of Figure 6, the most extreme cavitation taking place in the solvent with the lowest vapor pressure and viscosity combination. The correlation between cavitation and the deviation observed in the DPV confirms that the contribution from cavitational perturbation of the diffusion layer, from both bubble formation and microjetting, is significant in comparison with acoustic streaming under these conditions. Nevertheless, it is also clear that for mild ultrasonic stimulation, where the diffusion layer thickness is relatively large, then the Nernst diffusion model is physically realistic as testified by the good agreement between theory and experiment in the high diffusion layer thickness limit.

6. Conclusions

Chronoamperometric traces at insonated electrodes result in a characteristic transients comprised of sharp spikes superimposed on a background current that is much enhanced in comparison with the steady-state current observed under silent conditions. At a microelectrode, these spikes are caused by the collapse of an individual cavitational bubble in the vicinity of the electrode surface which casts a jet of electrolyte against it, bringing new electroactive material and giving the enhanced current observed on the transient. The size and multiplet nature of the spikes on the transient, show that they correspond to multiple collapses which occur at nearly similar times. The enhanced background current is attributable to acoustic streaming.

The size and frequency of the spikes on the microelectrode traces represent the amount and violence of the cavitation taking place in the solution. Calculation of the baseline current, the average current, and the standard deviation of the current allows a quantitative assessment of the amount of cavitation taking place relative to the mass transport contribution from acoustic streaming.

Differential pulse voltammetry was employed as a sensitive means, in parallel with chronoamperommetry, of exploring the nature of the diffusion layer prevailing under steady-state electrolysis at insonated macroelectrodes. The result is a physical model of an insonated electrode that may be described as a steady diffusion layer a few microns thick brought about by acoustic streaming, which is occasionally and randomly punctuated by a cavitational event the frequency and violence of which is dependent on the solvent and ultrasound power delivered, except at very short electrode-to-horn separation where the cavitational contribution becomes substantial.

The benefits of introducing ultrasound into electrochemical systems are wide ranging both in electroanalytical and electrosynthetic fields. Advancement in the field has opened up the need for a greater understanding of the relationship between cavitation and acoustic streaming, which is vital if greater selectivity in analysis and synthesis is to be pursued. As a result, this has recently provoked greater discussion about the origin and nature of these phenomena and factors that influence their operation in a range of physical conditions. The results described provide a greater understanding of acoustic streaming, which may prove to be as important and widespread as the well-established phenomenon of cavitation.

Acknowledgment. Financial support in the form of studentships from EPSRC (J.M.), BBSRC (J.L.H.) and the Basque Government (F.J. D.C.) is gratefully acknowledged.

References and Notes

(1) Walton, D. J.; Phull, S. S. *Adv. Sonochem.* **1996**, *4*, 205.
(2) Matsuda, K.; Atobe, M.; Nonaka, T. *Chem. Lett.* **1994**, *9*, 1619.
(3) Atobe, M.; Tonoi, T.; Nonaka, T. *Electrochem. Commun.* **1999**, *12*, 593.
(4) Mason, T. J.; Lorimer, J. P. Walton, D. J. *Ultrasonics* **1990**, *5*, 333.
(5) Akkermans, R. P.; Roberts, S. L.; Compton, R. G. *Chem. Commun.* **1999**, *12*, 1115.
(6) Marken, F.; Compton, R. G.; Buston, J. E. H.; Moloney, M. G. *Electroanalysis*, **1998**, *17*, 1188.
(7) Compton, R. G.; Marken, F.; Goeting, C. H.; McKeown, R. A. J.; Foord, J. S. *Chem. Comm.* **1998**, *19*, 1961.
(8) Marken, F.; Compton, R. G.; Davies, S. G.; Bull, S. D.; Thiemann, T.; Melo, M. L. S. E.; Neves, A. C.; Castillo, J.; Jung, C. G.; Fontana, A. *J. Chem. Soc., Perkin Trans. 2* **1997**, *10*, 2055,
(9) Madigan, N. A.; Murphy, T. J.; Fortune, J. M.; Hagan, C. R. S.; Coury, L. A., Jr. *Anal. Chem.* **1995**, *67*, 2781.
(10) Matysik, F. M.; Matysik, S.; Brett, A. M. O.; Brett, C. M. A. *Anal. Chem.* **1997**, *69*, 1651.
(11) Agra Gutiérrez, C.; Ball, J. C.; Compton, R. G. *J. Phys. Chem B* **1998**, *102*, 7028.
(12) Akkermans, R. P.; Ball, J. C.; Rebbitt, T. O.; Marken, F.; Compton, R. G. *Electrochim. Acta* **1998**, *23*, 3443.
(13) Agra-Gutiérrez, C.; Compton, R. G. *Electroanalysis* **1998**, *9*, 603.
(14) (a) Chiba, A.; Tani, T. Ouchi, Y. J. *Mater. Sci. Lett.* **1993**, *12*, 620; (b) Wu, W. C.; Chiba, A.; Nakanishi, K. *J. Mater. Sci. Lett.* **1993**, *12*, 794; c) Walker, C. T.; Walker, R. *J. Electrochem. Soc.* **1977**, *124*, 661.
(15) Pollet, B.; Lorimer, J. P.; Phull, S. S.; Hihn, J. Y. *Ultrasonics Sonochemistry*, **2000**, *7*, 69.
(16) Durant, A.; Del-Plancke, J. L.; Winand, R.; Reisse, J. *Tetrahedron Lett.* **1995**, *35*, 4257.
(17) Madigan, N. A.; Hagan, C. R. S.; Zhang, H.; Coury, L. A. *Ultrasonics Sonochem.* **1996**, *3*, S239.
(18) Birkin, P. R.; Silva-Martínez, S. *J. Chem. Soc., Chem. Commun.* **1995**, 1807.
(19) Marken, F.; Akkermans, R. P.; Compton, R. G. *J. Electroanal. Chem.* **1996**, *415*, 55.
(20) Nyborg, W. L. M., Mason, W. P., Eds.; *Physical Acoustics*; Academic Press: New York, 1965; p 265.
(21) Birkin, P. R.; Silva-Martínez, S. *J. Electroanal. Chem.* **1996**, *416*, 127.
(22) Rooney, J. A., Suslick, K. S., Eds.; *Ultrasound: Its Chemical, Physical, and Biological Effects*; VCH: New York, 1988; p 65.
(23) Hardcastle, J. L.; Ball, J. C.; Hong, Q.; Marken, F.; Compton, R. G. *Ultrasonics Sonochem.* **2000**, *1*, 7.
(24) Marken, F.; Akkermans, R. P.; Compton, R. G. *J. Electroanal. Chem.* **1996**, *415*, 55.
(25) Compton, R. G.; Eklund, J. C.; Page, S. D.; Mason, T. J.; Walton, D. J. *J. Applied Electrochem.* **1996**, *8*, 775.
(26) Anderson, J. L.; Moldoveanu, S. *J. Electroanal. Chem.* **1984**, *179*, 109.
(27) Laasonen, P. *Acta Math.* **1949**, *81*, 30917.
(28) Compton, R. G.; Pilkington, M. B. G.; Stearn, G. M. *J. Chem. Soc., Faraday Trans. 1* **1988**, *84*, 2155.
(29) Compton, R. G.; Melville, J. L. *J. Electroanal. Chem.* (in press).
(30) Pastore, L.; Magno, F.; Amatore, C. A. *J. Electroanal. Chem.* **1989**, *26*, 33.
(31) Fisher, A. C.; Compton, R. G. *J. Phys. Chem.* **1991**, *95*, 7538.
(32) Fisher, A. C.; Compton, R. G. *J. Appl. Electrochem.* **1992**, *22*, 38.
(33) Compton, R. G.; Laing, M. E.; Mason, D.; Northing, R. J.; Unwin, P. R. *Proc. R. Soc. London A* **1988**, *418*, 113.
(34) Albery, J. *Electrode kinetics*; Clarendon Press: Oxford, 1975.
(35) Hale, J. M. *J. Electroanal. Chem.* **1964**, *8*, 332.
(36) Hale, J. M. *J. Electroanal. Chem.* **1963**, *6*, 187.
(37) Marken, F.; Eklund, J. C.; Compton, R. G. *J. Electroanal. Chem.* **1995**, *395*, 335.
(38) Margulis, M. A.; Mal'tsev, A. N. *Russ. J. Phys. Chem.* **1969**, *43*, 592.
(39) Del Campo, F. J.; Neudeck, A.; Compton, R. G.; Marken, F. M. *J. Electroanal. Chem.* **1999**, *477*, 71.
(40) Klima, J.; Bernard, C.; Degrand, C. *J. Electroanal. Chem.* **1995**, *399*, 147.
(41) Peruisch, S. A.; Alkire, R. C. *J. Electrochem. Soc.* **1991**, *138*, 700.
(42) Peruisch, S. A.; Alkire, R. C. *J. Electrochem. Soc.* **1991**, *138*, 708.
(43) Leighton, T. G. *The Acoustic Bubble*; Academic Press: London, 1994.
(44) Goldfarb, D. L.; Corti, H. R.; Marken, F.; Compton, R. G. *J. Phys. Chem.* **1998**, *102*, 45.
(45) Burdin, F.; Tsochatzidis, N. A.; Guiraud, P., Wilhelm, A. M.; Delmas, H. *Ultrasonics Sonochem.* **1999**, *6*, 43.
(46) Laborde, J. L.; Bouyer, C.; Caltagirone, J. P.; Gerard, A. *Ultrasonics* **1998**, *36*, 589.